

Numerical Investigation of Heave and Pitch Motion Effects on Green Water Loading for a Floating Body

K. Ravindra Babu¹ · R. Datta¹ · A. Bhattacharyya¹

Received: 13 October 2017 / Accepted: 22 April 2019 / Published online: 22 October 2019
© Harbin Engineering University and Springer-Verlag GmbH Germany, part of Springer Nature 2019

Abstract

In this paper, the influence of heave and pitch motions on green water impact on the deck is numerically investigated. The vessel motions are determined using a potential theory based method and provided as input to finite volume based CFD computations of green water phenomenon. A dynamic mesh approach is adopted to determine instantaneous body positioning in the fluid domain. Detailed validation studies with published experimental results for 2D and 3D fixed vessel cases are initially performed to validate the present numerical approach before studying the moving vessel problem. The results show that inclusion of heave and pitch motion changes the disturbed wave field near the bow which influences the free surface as well as the impact loading due to green water. The effect of wave steepness on green water impact is also investigated and it is seen that the present numerical method is capable of capturing green water load. It is observed that the effects of vessel motions on green water load are not negligible and one should consider this effect too. The incorporation of vessel motions in the vertical plane affects the green water loading on the deck.

Keywords Green water impact pressure · Relative wave height · Vertical bow motion · Heave and pitch motions · Wave steepness · Floating body

1 Introduction

Green water loading or shipping of water on deck has been a major concern for the operation of ships and offshore structures because of its potential to impart significant structural damage. At a general level, depending on vessel type and operational conditions, the consequences could not only be local, but also global, i.e., the vessel may even capsize. The phenomenon is induced primarily by relative deck motion,

which is typically the motion of the forward part of the deck relative to the wave surface in head or bow sea waves. Green water impacts due to extreme waves are highly nonlinear in nature, and therefore it is extremely complicated to develop a proper analytical model for them. However, the study of green water impact is imperative as it may cause damage to certain parts of the vessel, such as bow, superstructures, and equipment on the deck. The well-known accident of M.V. Derbyshire in 1980 witnessed the destructive force of green water loading on the hatch covers, which ultimately led to the sinking of the ship. The Schiehallion FPSO was also damaged severely in November 1998 due to steep waves. This incident has resulted in considerable research interests subsequently in this domain. The magnitude of wave impact on the front of the bow is dominated by wave characteristics rather than by motions of ship relative to waves which is reported in Voogt et al. (2004). The local wave steepness is also critical in such impact loading due to green water.

The effect of green water loads is a well-researched topic which has been studied experimentally and mathematical models are also developed for prediction purpose. Buchner (1995) performed an experiment on green water loading on floating production, storage, and offloading units (FPSO) and found that it results in significant impact loading on the deck.

Article Highlights

- Effect of vessel motion on green water loading is investigated.
- A one way coupled model is developed for this purpose where effect of green water loading on vessel motion is ignored.
- The numerical model is validated against available published results in case of 2D and 3D cases to show the correctness of the present numerical model.
- Along with the vessel motion, the effect of wave steepness also considered. It is seen that both the parameters are critical and should consider for predicting the green water loading accurately.

✉ K. Ravindra Babu
ravindra.kudupudi@iitkgp.ac.in

¹ Department of Ocean Engineering & Naval Architecture,
IIT-Kharagpur, Kharagpur 721302, India

Gorf et al. (2000) carried out model scale experiments in the towing tank as well as full-scale experiments in a seaway with a wave buoy to understand the influence of wave steepness on green water impact. The effect of scaling was also investigated. Voogt and Buchner (2004) performed a series of experiments in order to study how wave steepness influences the impact pressure. It was reported that the experimental results were in better agreement with the calculations of relative bow height using second-order wave theory compared to those obtained from linear wave theory results. Greco et al. (2012) conducted experiments and extensive physical investigation for water on deck occurrence, where the rigid body motions and pressures at bow region (which is normally more affected by the shipping of water) has been measured.

In the context of theoretical development, the green water behavior on the deck was initially considered similar to the dam breaking problem (Buchner 1995). Later on, many advanced theories based on potential flow were developed. For example, a simplified nonlinear boundary element method was introduced by Buchner and Cozijn (1997), which was capable of representing the green water simulation on a two-dimensional body. Faltinsen et al. (2002) and Greco et al. (2004) developed a numerical model using 2D potential theory to study the green water loading on deck, superstructure, etc., in the head sea condition for zero forward speed. The numerical results were found to agree well with those obtained from the experiments unless wave breaking occurs. Greco and Lugni (2012) developed a 3D seakeeping numerical solver to account the effect of bottom slamming and green water loading. Greco et al. (2013) developed a 3D domain-decomposition for water-on-deck events which couples a linear potential flow seakeeping solver with a Navier-Stokes method in which nonlinear effects of heave and pitch motions are taken into account in the case of a ship without forwarding speed. They have also studied the effect of green water loading on parametric rolling numerically as well as experimentally (Greco et al. 2014, 2015).

More recently, with the availability of increased computational power, CFD-based methods are effectively employed for the numerical modeling of green water phenomenon. Lu et al. (2012) developed a time-domain simulation model using the volume of fluid method (VOF) to study the green water phenomena. Shibata and Koshizuka (2007) simulated green water impact on the deck for a 3D body using a moving particle semi-implicit method. Lee et al. (2009) predicted the green water impact on bow structure using the marker-density method which is capable of capturing the exact nonlinear free-surface efficiently. Le Touze et al. (2010) used smooth particle hydrodynamics (SPH) to simulate the effects of green water and the flooding effects due to water entering the mid-section of a vessel due to side collision. De Carvalho Silva and Rossi (2014) tested several commercial CFD solvers such as ANSYS CFX, ANSYS FLUENT, and STAR CCM+ adopting

the dam-breaking-type solution technique to predict green water loading on an FPSO. The simulation results reproduced the most critical pressure time series with approximately 5% deviations.

In the works mentioned above, the problem definition was limited to the modeling of the nonlinear free-surface waves causing an impact on deck. However, the effect coming from the vessel motion was ignored. Voogt and Buchner (2004) mentioned that the inclusion of ship motion is very important for the investigation of green water impact on the deck. Many researchers have tried to capture this effect in a simplified manner. For example, Nielsen and Mayer (2004) used a Navier-Stokes solver with a free-surface capturing scheme (i.e., VOF method) to model the green water effects on a moored FPSO exposed to head sea conditions. In that paper, the heave and pitch motion of the body is obtained by simplified analytical formula and the relative vertical bow motion is then considered for calculations of the green water impact. Kleefsman et al. (2005) used a potential flow solver to calculate vessel motion and free-surface boundaries which were used as the initial conditions for CFD computation of green water loading. Zhu et al. (2009) presented a numerical simulation scheme for both 2D and 3D numerical tanks to simulate the phenomenon of wave-ship interaction and green water on deck. The VOF method was used to capture the free-surface deformation of the green water process on a moored FPSO model in the head sea conditions. Here, the vessel motion was coupled with the CFD solver through dynamic mesh technique. Zhao et al. (2014) showed that the peak impact pressure due to green water on deck for a floating body decreases rapidly with the increase of its degree of freedom (DOF). The DOF was regulated by allowing the body to heave, sway, and roll, either as the only motion or as a combination of the three DOFs. Theilen et al. (2015) studied the green water loads on superstructures for a mega yacht. By using an efficient three-step approach to simulate green water loads. The solution approach taken by Theilen et al. (2015) is relatively less complicated for implementation, producing quite realistic results within engineering accuracy.

In general, CFD has certain advantages over potential flow-based solvers. For example, wave breaking can be modeled, which is challenging in a potential flow-based method. However, inclusion of vessel dynamics into the CFD solution is not trivial. However, limited literature is available where this effect is taken into account with sufficient details and CFD is used to capture the green water impact. In the present method, the body motion is calculated using a 3D panel method. Similar wave parameters and time synchronization are then created in CFD environment where the body motions are imported and then the problem of green water impact is solved. In Table 1, a brief overview of published research work regarding green water is given and the present work is shown in perspective of that.

Table 1 A brief overview of significant published research on green water loading

Research	Potential flow theory	CFD	2D fixed	3D fixed	Vertical bow motion	Coupled heave and pitch motion	Wave steepness	Validation with experiments
Buchner (1995)	Y	N	N	Y	N	Y	N	Y
Cozijn (1995) and Buchner and Cozijn (1997)	Y	N	Y	N	N	N	N	N
Faltinsen et al. (2002)	Y	N	Y	Y	N	N	N	Y
Voogt et al. (2004)	Y	N	N	Y	N	N	Y	Y
Nielsen and Mayer (2004)	N	Y	Y	Y	Y	N	N	Y
Shibata and Koshizuka (2007)	N	N	N	Y	N	N	N	Y
Zhu et al. (2009)	N	Y	Y	N	N	Y	N	Y
Le Touze et al. (2010)	Y	Y	Y	Y	N	N	N	Y
Greco et al. (2012)	Y	Y	Y	Y	N	Y	Y	Y
Lee et al. (2012)	N	Y	N	Y	N	N	Y	Y
Zhao et al. (2014)	N	Y	Y	N	N	N	N	Y
Theilen et al. (2015)	N	Y	N	N	N	N	N	N
Present work	N	Y	Y	Y	Y	Y	Y	Y

The present work can be considered as an extension of the work proposed by Zhu et al. (2009) and Zhao et al. (2014), where both two-dimensional and three-dimensional numerical wave tanks are used to simulate the phenomenon of wave-ship interaction and green water on deck. Impact pressure on the deck is calculated by taking vertical bow motion as well as exact body motion with the help of dynamic mesh technique. For this purpose, the continuity equation and Navier-Stokes equations are solved in the fluid domain, and a VOF method is used to capture the nonlinear exact free-surface elevation. Heave and pitch motions are calculated within linear potential theory using a 3D time domain panel method and provided as an input to the commercial CFD solver (ANSYS fluent) which calculates the impact loading due green water for the vessel in prescribed motion. The CFD-based approach presented in this paper is validated with available published numerical and experimental results for the case of fixed vessel. Further, the influence of vessel motion, i.e., heave and pitch, and wave steepness on green water loading is also systematically investigated.

2 Mathematical Formulation

In the present study, the fluid is assumed to be incompressible, homogenous, and flow is irrotational. The motion of the body calculated a priori is assumed to be linear. Since there is a phase difference between the body motion and that of the incident wave, it is important to keep the same phase between the wave generated in the numerical wave tank and the body motion.

2.1 Governing Equations

The numerical approach involves discretizing the spatial domain into finite control volumes (for example, Versteeg and

Malalasekera 2007) using a suitable mesh. The equations of continuity and momentum conservation can be written as follows:

$$\frac{\partial \rho}{\partial t} + \frac{\partial(\rho u)}{\partial x} + \frac{\partial(\rho v)}{\partial y} + \frac{\partial(\rho w)}{\partial z} = 0 \quad (1)$$

$$\rho \left(\frac{\partial(u)}{\partial t} + u \frac{\partial(u)}{\partial x} + v \frac{\partial(u)}{\partial y} + w \frac{\partial(u)}{\partial z} \right) = \mu \left[\frac{\partial^2 u}{\partial x^2} + \frac{\partial^2 u}{\partial y^2} + \frac{\partial^2 u}{\partial z^2} \right] - \frac{\partial p}{\partial x} \quad (2)$$

$$\rho \left(\frac{\partial(v)}{\partial t} + u \frac{\partial(v)}{\partial x} + v \frac{\partial(v)}{\partial y} + w \frac{\partial(v)}{\partial z} \right) = \mu \left[\frac{\partial^2 v}{\partial x^2} + \frac{\partial^2 v}{\partial y^2} + \frac{\partial^2 v}{\partial z^2} \right] - \frac{\partial p}{\partial y} \quad (3)$$

$$\rho \left(\frac{\partial(w)}{\partial t} + u \frac{\partial(w)}{\partial x} + v \frac{\partial(w)}{\partial y} + w \frac{\partial(w)}{\partial z} \right) = \mu \left[\frac{\partial^2 w}{\partial x^2} + \frac{\partial^2 w}{\partial y^2} + \frac{\partial^2 w}{\partial z^2} \right] - \frac{\partial p}{\partial z} - \rho g \quad (4)$$

where u, v , and w denote the velocity components of the fluid particles in the x -, y -, and z -directions, g is the gravitational acceleration. Here, z is the vertical upward axis (Fig. 1).

The VOF method (Hirt and Nichols 1981) is adopted to capture the free-surface deformation. The equations can be written as follows:

$$\rho = \sum_{q=1}^2 a_q \rho_q \quad (5)$$

$$\frac{\partial a_q}{\partial t} + \frac{\partial(u a_q)}{\partial x} + \frac{\partial(v a_q)}{\partial y} + \frac{\partial(w a_q)}{\partial z} = 0, q = 1, 2 \quad (6)$$

$$\sum_{q=1}^2 a_q = 1 \quad (7)$$

where $q = 1$ and 2 denote the air phase and the water phase, respectively. ρ is the volume-fraction-averaged density, a_q is the volume fraction, denoting the ratio of the volume of the q th phase fluid occupying a cell, and μ is the volume-fraction-averaged dynamic viscosity similarly defined as the volume-fraction-averaged density. Here, an impermeability condition is enforced at the hull surface.

In this paper, a SIMPLE scheme is employed for pressure-velocity coupling. To discretize the convective term in the Eqs. (2)–(4) for transport of the volume fraction, compressive interface scheme is used. It uses an implicit representation of the free surface based on the volume fractions. The open channel wave boundary condition is used to generate the incident wave as a regular wave.

2.2 Mesh Generation and Dynamic Mesh Technique

In this paper, two aspects have been taken into consideration while constructing the computational grid. Firstly, the generation of regular head waves from the inlet, and secondly, incorporation of vessel motions (calculated using potential flow) into the CFD solver. A fine grid is used near the free surface for capturing the incident wave kinematics.

As shown in Fig. 1, the computational domain consists of four zones in the x -direction. The length of each zone is estimated as a function of the wavelength. In the wave generation zone, to avoid wave damping, fine grids are used. Similarly, in the critical domain, where the flow parameter gradients are higher, dense grids are used. However, for the transition zone and damping zone, a relatively coarse grid is used. In Table 2, the approximate grid size is given as a function of wavelength for the different zones.

Since the fluid flow characteristics are computed considering the motions of the body, an accurate and efficient dynamic meshing technique is employed to calculate the velocity and pressure fields. In order to capture the wave profile around the bow, the fluid domain is decomposed into two parts—near field and far field. It is assumed that the radiated and diffracted waves are damped in the damping zone, which is clearly illustrated in Fig. 1. In order to incorporate these phenomena

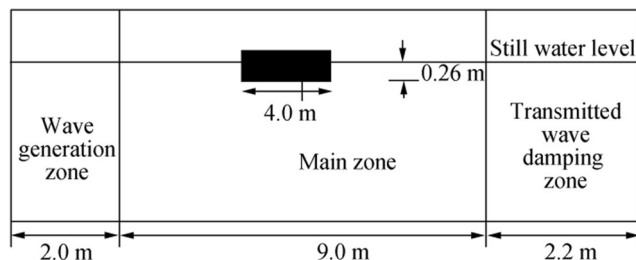


Fig. 1 Numerical wave tank

Table 2 Grid generation scheme

Zone	Grid size in x -direction in the form of wavelength
Wave generation zone	$\lambda/200$
Main zone	$\lambda/436$
Transition zone	$\lambda/100$
Damping zone	$\lambda/45$

numerically, a proper damping scheme is employed and a marching algorithm is used to connect the two domains. The damping scheme is discussed in the following section. Since the oscillation of the body is assumed to be small, a hexa-mesh is used in this paper for solution purpose. However, for larger motions, the hybrid mesh should be used. Since the mesh is attached to the body and moving with it, proper care should be taken while creating the mesh so that normal velocity of the body and the fluid domain attached to the body remain same. This technique is graphically illustrated in Fig. 2, where the near field mesh is shown for a semi-circular body.

To account for motion displacement, the dynamic mesh based on diffusion-based smoothing technique (refer ANSYS Fluent 2017 manual) and dynamic layer technique are used. The cell-volume-based diffusion equation is given by the following:

$$\gamma = \frac{1}{V^\alpha} \quad (8)$$

where γ is the diffusion coefficient, V is the normalized cell volume, and α is the diffusion parameter. The theory behind the proposed damping technique is explained in many sources (Park et al. 1999; Zwart et al. 2007) and not mentioned here.

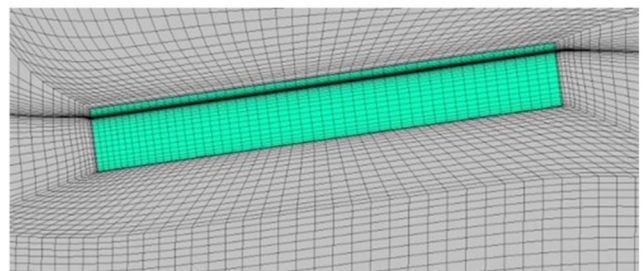
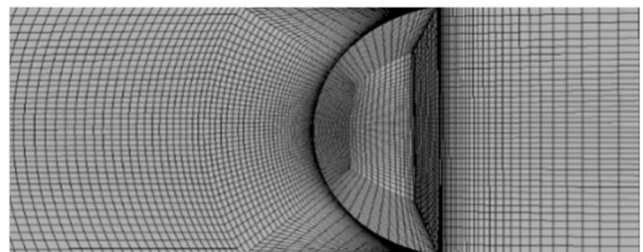


Fig. 2 Mesh around body and dynamic mesh in simulation

In the diffusion-based smoothing method, the mesh nodes move in response to the displacement of boundaries by calculating a mesh velocity using the diffusion Eq (8) which controls the diffusion of boundary motion into the interior of the fluid domain as a function of cell size. In the dynamic layer technique, the layers of cells around the body boundary move with the body, i.e., the body boundary condition is explicitly enforced. This means that a new layer of the mesh inside the fluid domain is added by applying a face zone with adjacent successive fluid layer. The deformation of the mesh is captured subsequently. The details of this method can be found out in ANSYS fluent (2017).

The dynamic mesh is extremely sensitive and requires proper attention to efficiently capture the body motions. Figure 3 represents the failure of the mesh deformation when the vessel is heaving and pitching. Therefore, to overcome this problem, proper refinement for spatial parameters is made in both horizontal and vertical directions. Figure 4 shows the mesh deformation for a rectangular barge after incorporating the refinement in several longitudinal planes (x - z planes).

2.3 Damping Scheme

In the present work, numerical beach treatment is used to subdue the numerical reflection of the propagating waves at the outlet boundary by adding a dampening sink term. Referring to the co-ordinate system stated in Fig. 1, the sink momentum term ' S ' is computed using the standard momentum sink equation:

$$S = - \left[C_1 \rho V + \frac{1}{2} C_2 \rho |V| |V| \right] f(z) f(x) \quad (9)$$

In Eq. (9), C_1 and C_2 represent the linear and quadratic damping factor. V is the velocity along the z -direction, $f(x)$ and $f(z)$ are the damping functions in x - and z -directions respectively.

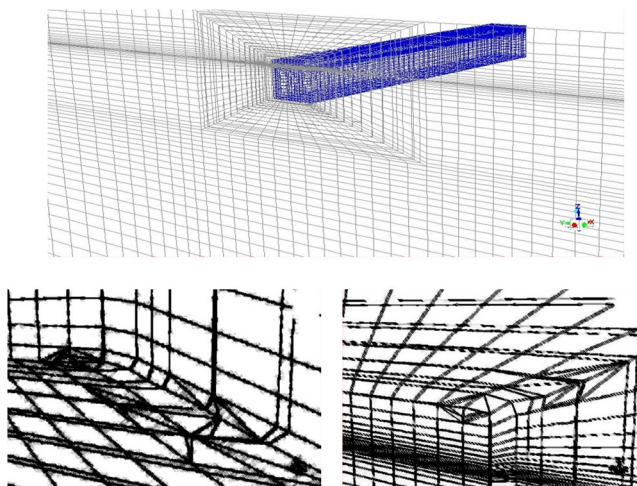


Fig. 3 Mesh deformation failure for the vessel in motion

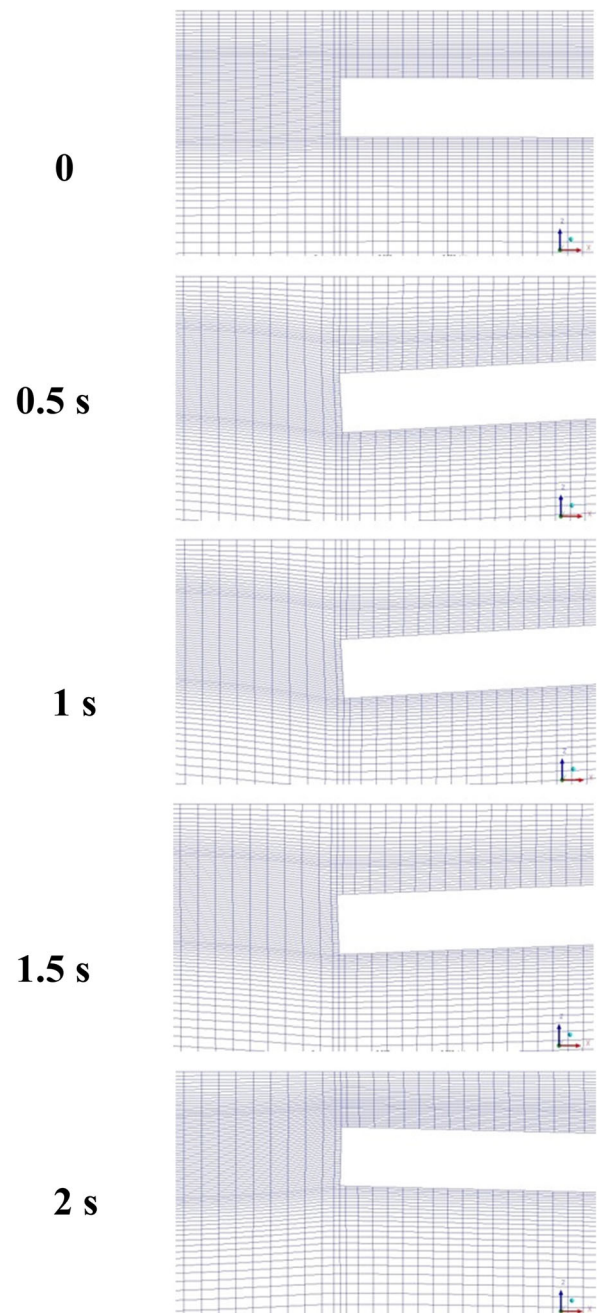


Fig. 4 Dynamic mesh deformation for a rectangular barge. The snapshots are enumerated as time increases at a time interval of 0.5 s

The damping functions $f(x)$ and $f(z)$ are given by the following:

$$f(x) = (r_x)^2 \quad (10)$$

$$f(z) = 1 - r_z \quad (11)$$

The scaling factors r_x and r_z are defined by the following:

$$r_x = \frac{X - X_s}{X_e - X_s} \quad (12)$$



Fig. 5 Damping scheme applied at the outlet zone (right side)

$$r_Z = \frac{Z - Z_{fs}}{Z_b - Z_{fs}} \quad (13)$$

In Eq. (12), X_s and X_e are the start and endpoints of the damping zone in the x -direction and in Eq. (13), Z_b and Z_{fs} are the free surface and bottom level along the z -direction. The selection of the damping region is important as too high or too low damping could affect the wave profiles in the zero-damping zone. In Fig. 5, implementation of the damping scheme is shown. From the figure, it can be seen that the proposed damping scheme is effective in damping the wave at the domain outlet.

3 Case Studies

The present numerical model is initially validated with experimental results for 2D FPSO given by Greco (2001), and for 3D FPSO given by Shibata and Koshizuka (2007). Subsequently, a rectangular barge is taken to compute the green water loading for heave and pitch motions. Considering this, two cases are investigated: (i) A body with relative bow motion, i.e., completely ignoring the pitching effect which is undergoing heaving motion only; however, the motion of the body is defined as $Z_v = Z - x_p \cdot \theta$, where Z_v is vertical bow motion, Z is the heaving motion, and θ is defined as pitch motion and x_p is the position where impact load is calculated; (ii) taking the actual configuration of the body after considering the heave and pitch motion. The impact pressure results presented in this paper are non-dimensionalized using the expression $(\rho g H)$, where ' H ' is wave height.

3.1 A 2-Dimensional Body (FPSO)

3.1.1 Problem Setup

Figure 6 shows the FPSO model along with the wave probe-WP, located at 0.8 m from the wave inlet. The wave elevation on the deck which is measured at WL₁ and WL₂ and the pressure is computed at PR₁ which is located at 0.2275 m away from the bow on superstructure on deck. The details of

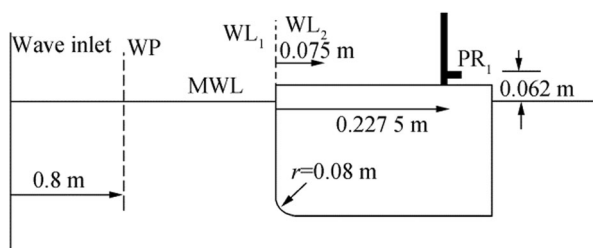


Fig. 6 FPSO model

the tank and the model particulars are given in Table 3. Results obtained from the present work are mentioned as “Present” in the comparison plots shown in this paper.

3.1.2 Results

The design mesh used in this work is based on a grid convergence study, where the maximum impact pressure is used as the indicator function plotted against the number of cells in the domain (Fig. 7(a)) and for the numerical convergence for the study on the body motions for pressure and for the wave elevation on the deck has been plotted in Fig. 7(b), (c). It is observed that good convergence of results is obtained using 85 000 cells for the 2D domain. Around the body, the cell size is 0.02 times freeboard (f), i.e., $0.02f$. In the damping zone, i.e., near the pressure outlet it is $0.4f$.

The wave elevation at WP is calculated to check the quality of the generated incident waves. Figure 8 shows the time history of the wave elevation at WP. It may be observed that slight nonlinearity arises at WP. This could be due to the superposition of the incident wave and the reflected from the bow of the structure. A similar pattern is observed in Greco (2001) as well. However, due to the incorporation of the damping scheme, a quite stable incident wave train is generated in the wave-making zone. This indicates that the present numerical scheme is effective for simulation of the incident wave.

The time histories of the wave height at probes WL₁ and WL₂ are shown in Fig. 9(a), (b) and compared with experimental results by Greco (2001). It may be interesting to note that two significant peaks appear in time histories by Greco (2001) and the second one is larger than that of the first one. According to Greco (2001), this happens because when the first incident wave peak approaches the bow of the structure, the wave height of the front of the bow is increased due to wave reflection. Therefore, when the next incident wave approaches to the bow, it is superimposed with the reflected wave and becomes even higher at the front of the bow. It is interesting to note that, the present numerical CFD model is able to capture the phenomenon. To understand this, a comparison of the time history of wave elevation at WP is made with those at the two reference points on the deck (WL₁ and WL₂) in Fig. 10. The time differences between the first and second peak for the points

Table 3 Input parameters for green water loading (2D case)

Wavelength	λ	2.0 m
Wave height	H	0.16 m
Acceleration due to gravity	g	9.8 m/s ²
Freeboard	f	0.05 m

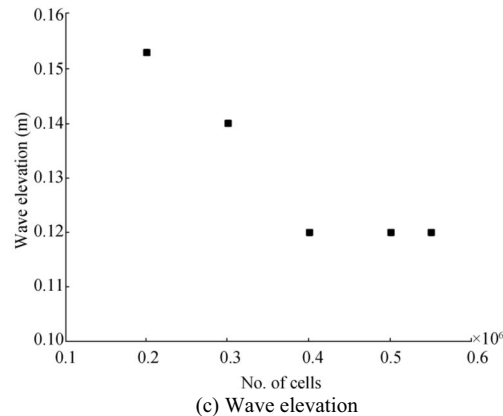
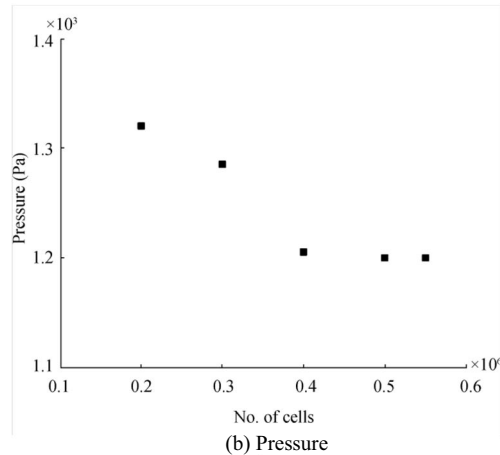
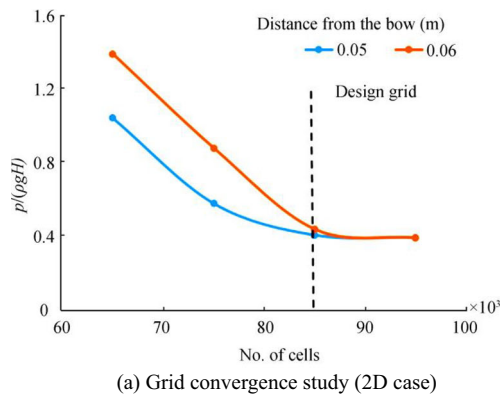


Fig. 7 Grid convergence study on the body motions on deck for pressure and wave elevation

WP, WL₁, and WL₂ are indicated as '*t*₁', '*t*₂' and '*t*₃' respectively. It is observed that the values for WL₁ and WL₂ differ from that of WP by less than 5%. This indicates the time synchronization of the successive peaks obtained for the incident wave elevation at WP with the wave elevations at WL₁ and WL₂ on the vessel. Also, the highest wave elevation is observed for the second peak at WL₁ where the effects of bow reflection should be more prominent.

Figure 11 shows a comparison of the time history of impact pressure at probe PR₁ between experimental and numerical

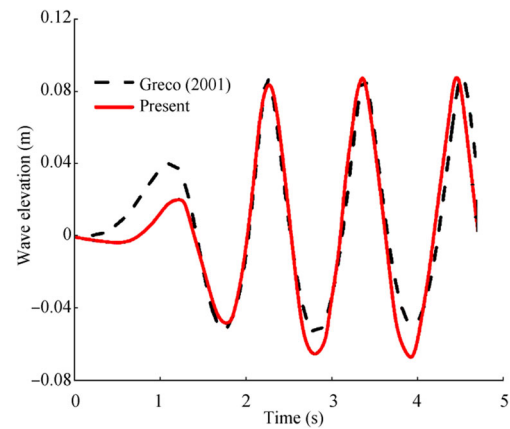


Fig. 8 Comparison of wave kinematics at wave probe WP

calculations. Here also, two peaks can be observed for impact pressures which are in good comparison with the experimental results. The first one occurs due to the initial impact and the second one could be when the water starts to come down from the mounted structure after reaching the maximum height.

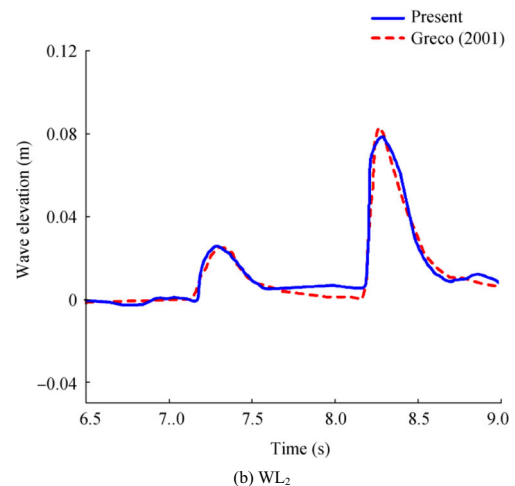
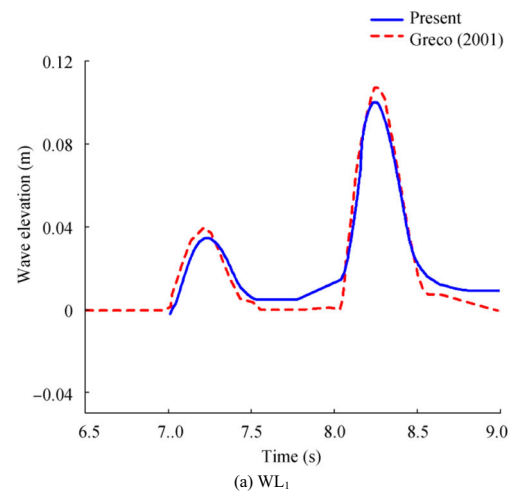


Fig. 9 Time history of waves at probe WL₁ (located at the front end of the bow) and WL₂ (located 0.075 m from the bow end)

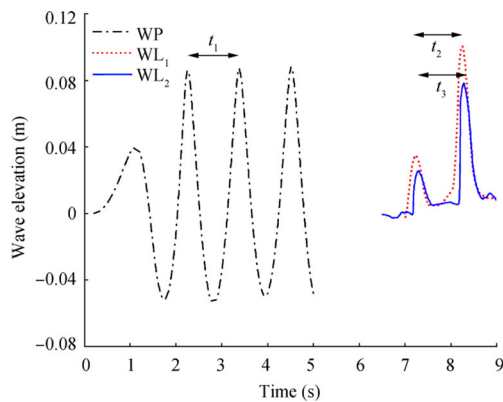


Fig. 10 Time histories of wave elevation at WP, WL₁, and WL₂

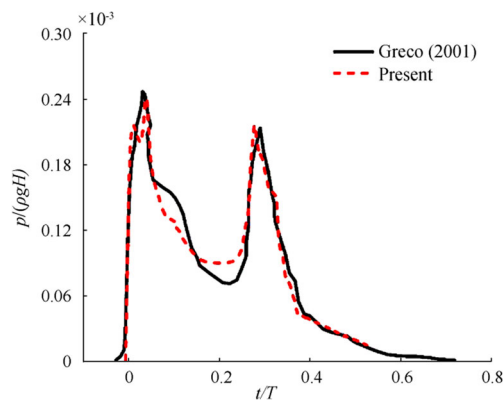


Fig. 11 Time history of impact pressure at probe PR₁ on the mounted structure

From the 2D results, it can be seen that the proposed numerical model works well for the simpler 2D body and is able to capture the flow physics. In the following sections, a fixed 3D body is taken for the validation for the present numerical model.

3.2 A Fixed 3-Dimensional Body

3.2.1 Problem Setup

Initially, steepness check has been done for the present numerical model compared with results obtained from Lee et al. (2012) and the model setup for computing the green water impact on a 3D body has been adopted from Shibata and Koshizuka (2007). The input parameters to perform the green water loading are given in Table 4. Figure 12 shows the

Table 4 Input parameters for green water loading (3D case, fixed vessel)

Wavelength λ (m)	1.37
Wave height H (m)	0.10
Acceleration due to gravity g (m/s ²)	9.81
Freeboard f (m)	0.05

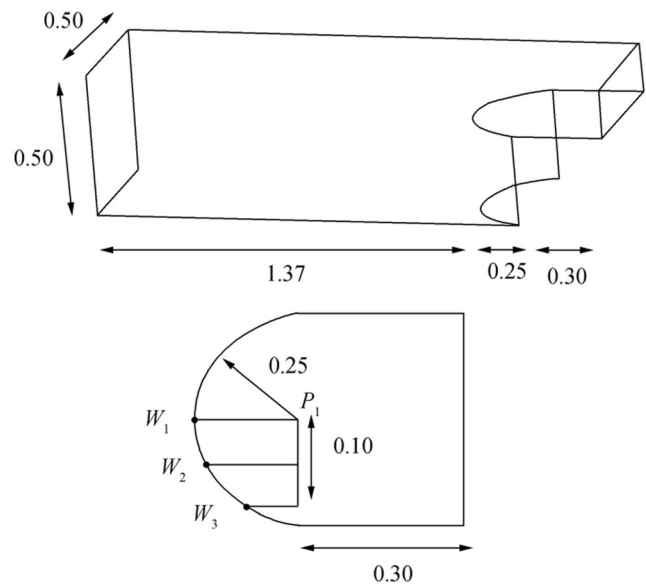


Fig. 12 Principal dimensions of the numerical tank domain

principal dimensions of the numerical tank domain with wave probes W₁, W₂, and W₃, and Fig. 13 shows the domain grid. The approximate size of the cells used in the different zones (ref. Figure 1) is given in Table 5.

A schematic diagram is given in Fig. 14 to explain the subdivision of the domain in more details. In Fig. 14, “A” and “B” represent the inlet and outlet boundaries respectively, whereas the parts “C” and “D” represent the sidewall and the body respectively. A finer mesh is created around the body to capture the wave-body interaction and the mesh is stretched towards “A” and “B” using a hyperbolic stretching function.

3.2.2 Results

The result from present numerical model is compared with that of the experiment done by Lee et al. (2012) for different steepness at $\lambda/L = 2$. The detailed description of the model, dimension is given in Lee et al. (2012), and thus not reported in this paper. The results are plotted in Fig. 15. The comparison shows a very good agreement with experiment results.

For the fixed vessel case, both the wave height and the impact pressure on the deck structure are obtained. Figure 16 shows the time histories of the wave heights at the three probes. The results from the present method are

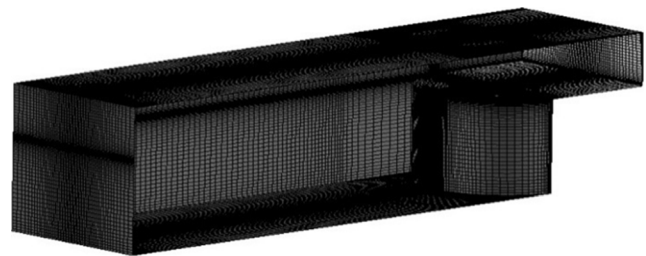


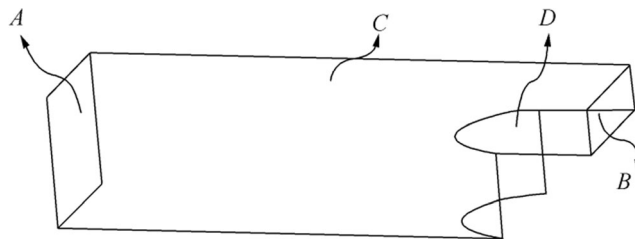
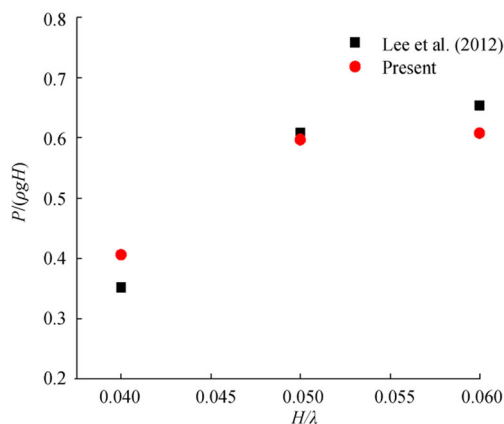
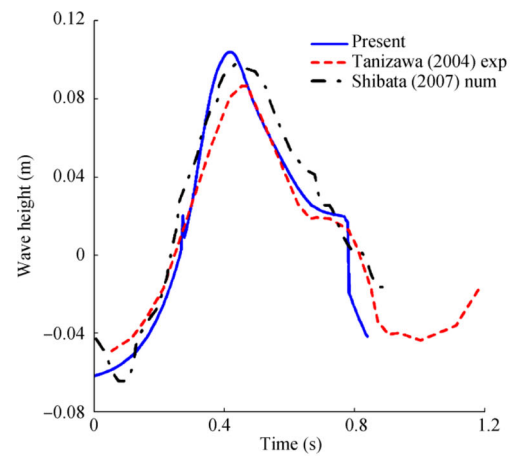
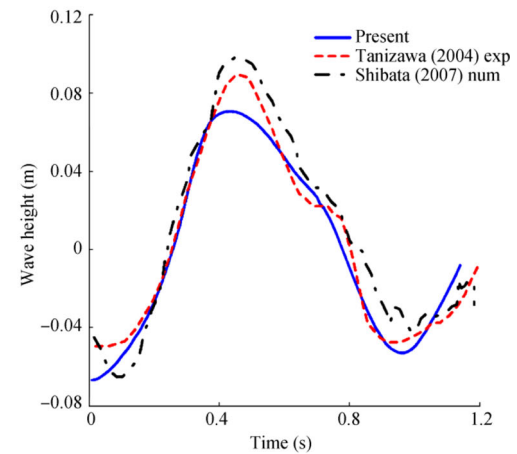
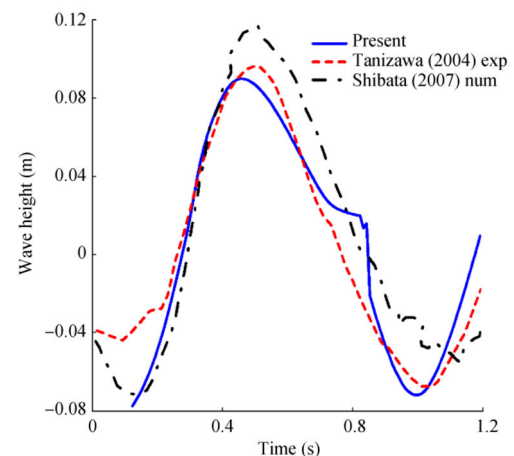
Fig. 13 Domain grid

Table 5 Mesh information (m)

Zone	Grid size in z -direction
Water zone	0.02
Free-surface zone	0.001
Air zone	0.02

compared with numerical results reported by Shibata and Koshizuka (2007) and referred to as “Shibata and Koshizuka (2007) num.” The experimental results are taken from the paper by Tanizawa et al. (2004) and referred here as “Tanizawa et al. (2004) exp.” An overall good agreement with both the numerical and experimental results can be observed from Fig. 16, except around 2%–3% variations in the peak value. Also, it can be noted that only a single peak has occurred in this case. Since there is no mounted structure in the bow, there is no wave reflection to disturb the incident wave flow.

Next, the impact pressure is calculated at the location of 0.25 m from the front end of the bow where the pressure gauge is placed in the experiments at P_1 . The time histories of the impact pressure in one wave cycle are compared in Fig. 17. Here, also, a similar trend is observed except some differences near the peak value and a milder slope in the pressure rise compared to the experimental results. This may be due to underestimation of the impact pressure in CFD calculations or due to experimental uncertainties.

**Fig. 14** A schematic diagram of domain**Fig. 15** Comparison of wave steepness for pressure peaks at P_{11} location for Rect0 model (Lee et al. 2012)(a) W_1 (b) W_2 (c) W_3 **Fig. 16** Time histories of the wave heights at W_1 , W_2 , and W_3

According to Shibata and Koshizuka (2007), the numerical model has assumed the front part of the bow do not provide any frictional force to the fluid, i.e., the fluid slips through the deck surface after water splashes on the deck. However, in the experiment, some frictional forces may develop due to green

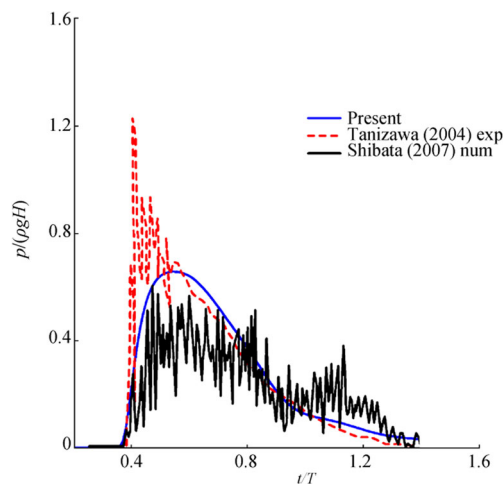


Fig. 17 Time history of the impact pressure

water loads on the deck and concentrated on the leading edge. Owing to this concentration of the water on the leading part of the deck, the pressure suddenly increased in the experiment. The present numerical model, as well as the numerical model proposed by Shibata (2007) did not consider this effect because for green water loading frictional force is assumed to be negligible. This has typically been the case, for example, Zhu et al. (2009) and Silva et al. (2016). The visualized images of the calculated green water behavior of both “Present” and “Shibata (2007) num” presented in Fig. 18 are similar in nature, and these results have qualitatively been validated with the experiments performed by Shibata and Koshizuka (2007).

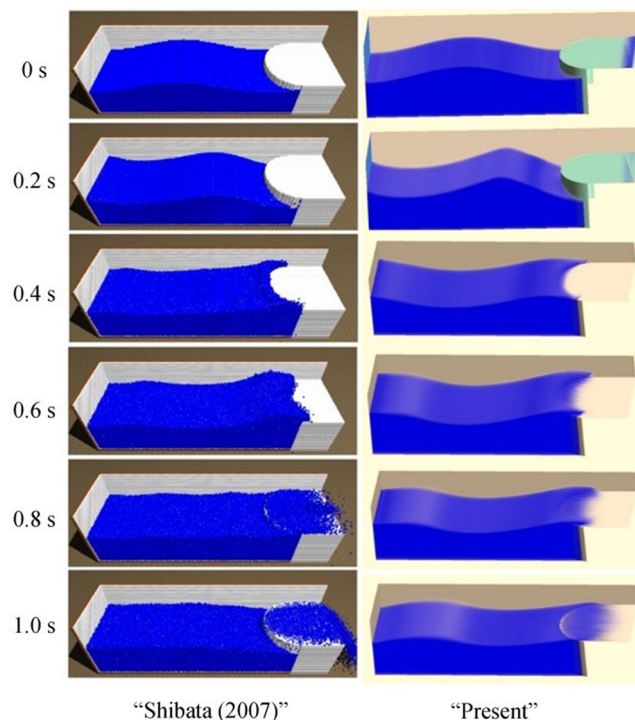


Fig. 18 Visualization of the shipping water behavior

These comparisons establish the effectiveness of the present method for application to complex 3D problems considering green water loading.

3.3 A 3-Dimensional Body (FPSO) Oscillating in Waves

In this section, a floating body is taken for the analysis, i.e., the body is undergoing heave and pitch motion. The motion results are obtained a priori using 3D time domain panel method and used in CFD solver. The linear and nonlinear versions of the motion code are already validated and the results are available in published literature (Datta et al. 2011, Datta and Fonseca 2013, Sengupta et al. 2016). In the present study, the CFD model is not coupled with BEM because it is assumed that green water load will not affect the global motion. To justify this assumption, the maximum amplitude of the green water load is compared with that of the exciting force. Table 6 shows that for different λ/L ratio, F_t represents non-dimensional exciting force, which has been calculated using the potential flow solver and F_{gw} shows non-dimensional peak green water force from the CFD, i.e., green water pressure has been considered on a small strip with a unit length and a width of beam of the vessel. Both the forces are non-dimensionalized by $\rho g V_L$. In this expression, ρ represents the density of the seawater, g represents the acceleration due to gravity at the Earth's surface, and V_L represents the volume of the vessel in static condition. The third column represents $\left(\frac{F_{gw}}{F_t}\right) \times 100\%$, i.e., it shows the ratio between the two forces expressed as percentage. From Table 6, it is observed that the green water force is typically less than 1% of the exciting force, except for the case $\lambda/L = 1$, where it is 5.7% of F_t . This gives an idea of the effects/errors due to green water loads for calculation of vessel motion.

3.3.1 Problem Setup

In the previous two sections, the effectiveness and efficiency of the present numerical model are checked for the fixed vessel case and found satisfactory. In this section, the main physical problem is thoroughly addressed, i.e., investigate the

Table 6 Percentage peak difference for non-dimensional green water force with respect to exciting force

λ/L	F_t	F_{gw}	Percentage
0.75	13.84	0.11	0.8
1	9.51	0.54	5.69
1.5	44	0.45	1.03
2	72.5	0.26	0.36
2.5	90.39	0.22	0.24

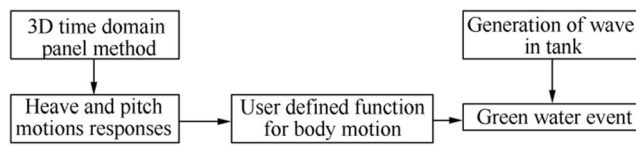


Fig. 19 Flow chart of green water event for coupled motion

vessel motion on green water impact. In order to see the effect, three different scenarios are considered:

- Case1 (Fixed vessel case): Assuming the body is not moving from its initial position and then impact loading due to shipping of water on deck is computed.
- Case2 (Vertical bow motion): Body is with vertical bow motion which is essentially the coupled heave and pitch motion, but 3D effect or rotation is not considered.
- Case3 (Exact): Body with heave and pitch motions (i.e., exact body configuration).

Here, the vertical motions are critical around the λ/L ratio of 1, the wavelength chosen is equal to the length of the vessel. Also, this choice of wavelength is based on previous studies (Zhu et al. 2009) for a 3D body. In the proposed method, it is assumed that vessel motion is only affecting the green water loading, but not vice versa, i.e., the green water loading does not affect the global motions significantly. Under these assumptions, one can decouple the above problem as given in the flow chart (Fig. 19) where heave, pitch, and the corresponding vertical motion can be obtained separately and provided as input to the CFD solver. The heave and pitch motion are pre-computed using a well-established time-domain panel method developed in-house (Datta et al. 2011; Datta and Fonseca 2013; Sengupta et al. 2016). The vertical bow motion $v(t)$ at any point on deck at a distance x_p from the center of gravity can be given by the simple equation as follows:

$$v(t) = z(t) - x_p \cdot \theta(t) \quad (14)$$

where $z(t)$ and $\theta(t)$ are the instantaneous heave and pitch displacements calculated from the time domain panel code.

A rectangular box or barge type structure is taken for the analysis. The model particulars and input parameters are given in Table 7. Figure 20 shows the computational mesh. The points H_1 , H_2 , and H_3 signify the location of the probes where resulting water height on the deck are measured, while impact pressure is calculated at the points P_1 , P_2 , and P_3 . Figure 21(a)

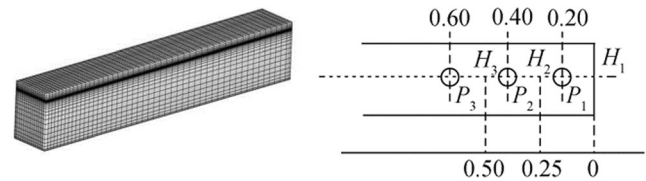
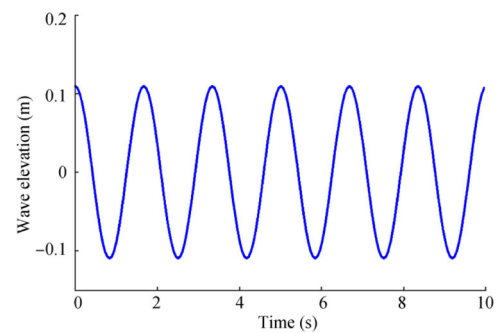


Fig. 20 Meshing of the barge and schematic diagram

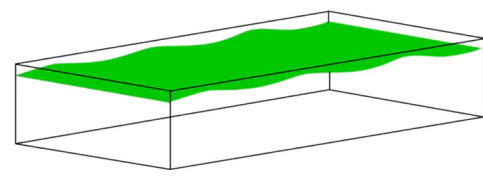
shows the wave profile at H_1 when the body is absent. Fig. 21(b) shows the wave profile along the horizontal axis before it damps down due to numerical beach treatment. Figure 22 shows the heave and pitch motions of the body at the CG and vertical bow motion at the point P_1 corresponding to the wave condition given in Table 7.

3.3.2 Results

An initial study is done to check if the present model can capture the near field disturbances caused by the vessel motion. This is important because while capturing the exact free surface, the radiated wave and diffracted wavefield should be accounted for, and therefore, the numerical models should be



(a) Time history of the wave profile



(b) Visualization of the wave

Fig. 21 Time history of the wave profile and visualization of the wave

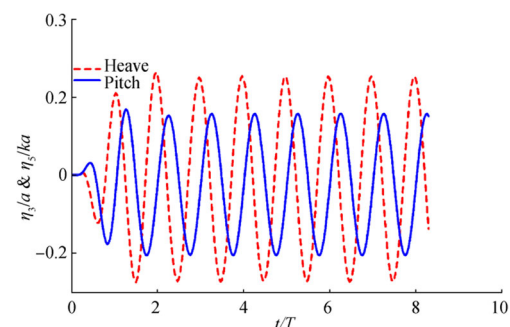


Fig. 22 Heave and pitch motion of body

Table 7 Model particulars and input parameters for floating barge (m)

Length	4.00
Beam	0.30
Draft	0.26
Depth	0.30
Wavelength	4.36

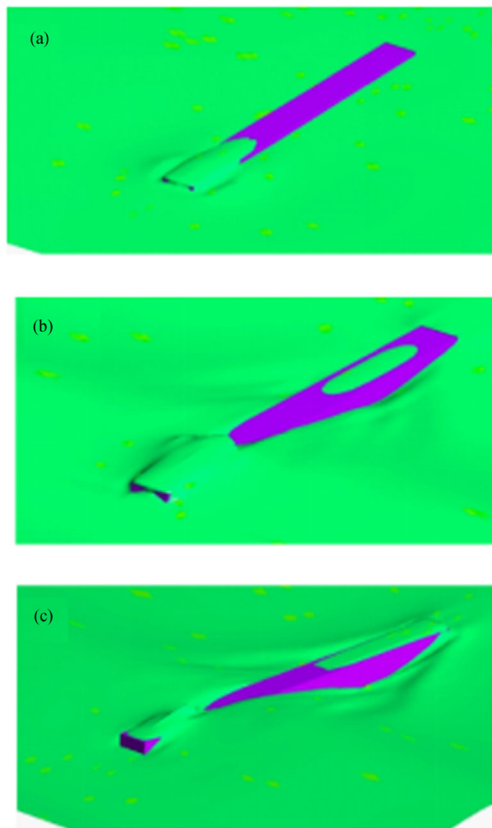


Fig. 23 Free surface around the body for **a** body oscillation in calm water, **b** body fixed under wave, and **c** heaving and pitching under waves

able to capture the total disturbed wavefield near the bow area of the vessel. To illustrate this, three free-surface configurations are shown in Fig. 23(a). The vessel is oscillating in still water, i.e., the radiated wave field, (b). The free-surface wave hits the fixed vessel, i.e.; the diffracted wave field, and (c) The combination of (a) and (b), i.e., the body is oscillating under linear wave, and it is denoted as radiated-diffracted wave. From Fig. 23, it can be seen that these three wavefields are quite different from each other which may be due to different boundary conditions for the three cases. For example, in case

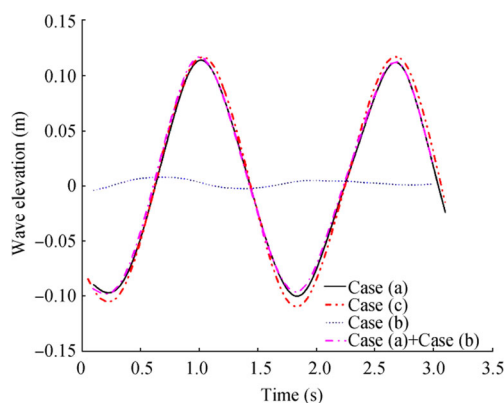
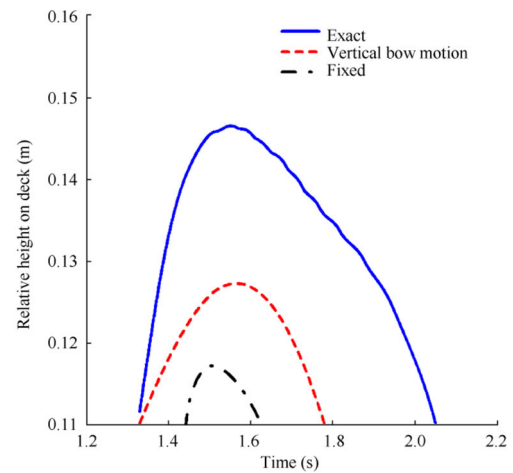
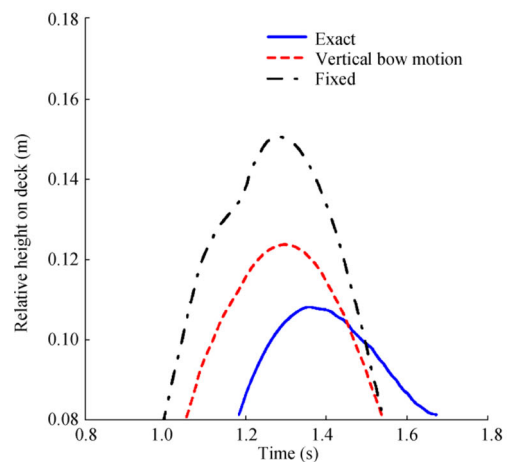


Fig. 24 Time history for the different cases

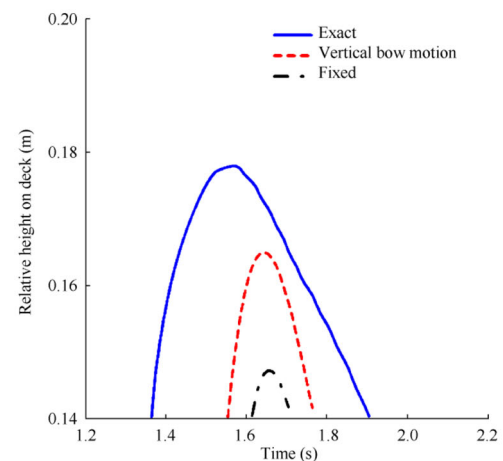
(a), a rigid wall motion is imposed on still water which is analogous to the radiation boundary condition. In case (b), the body is considered on a fixed rigid wall under waves which is analogous to the diffraction boundary condition, i.e., the normal velocity of the fluid particle attached to the



(a) H_1



(b) H_2



(c) H_3

Fig. 25 Relative height of the wave at H_1 , H_2 , and H_3

body is zero. In case (c), both (a) and (b) are combined, i.e., a rigid wall is moving under the wave, which may be considered to have the same boundary condition as for the radiation-diffraction case. For an accurate validation of the superposition principle, the diffracted and radiated waves should be added to the incident wave. To ensure this superposition principle, a wave probe is kept near the bow (0.3 m near to the bow) and time signal for the generated wave for case (a), (b), and (c) is captured. Figure 24 shows the time history for the radiated wave (case (a)), diffracted wave (case (b)), radiated–diffracted wave (case (c)) and superposition of radiated and diffracted wave. From the figure, it may be noted that the time history plot for case (c) is almost similar to case (a) + case (b) which validates the superposition principle.

Figure 25 (a), (b), and (c) represents the relative height of the wave with respect to the deck at three different locations. It is seen from Fig. 25 that relative height of “Exact” and “Vertical bow motion” cases will be different from the “Fixed” case as expected. Interestingly, relative wave height of “Vertical bow motion” is different from “Exact” case even though the incident wave profile is similar in both the cases. This can be explained in light of the difference in motion configurations between the two cases, resulting in differences in the respective disturbed wave fields. These phenomena can be observed more clearly in Fig. 26 where visualization of the wave-body kinematics is presented. From the figure, one may observe that at 1.2 s and 1.6 s, there are minor differences in the free surface due to different body configuration for “Vertical bow motion” and “Exact” cases along the horizontal axis.

Figure 27 (a), (b), and (c) presents the corresponding green water pressure obtained at three locations on the deck (refer Fig. 19). It is observed that the impact pressure is always higher for “Exact” case for all the points. This could be because of the deck acceleration as well as phase of the body motion with respect to the wave. From Figs. 21(a) and 22, one can observe that the heave and pitch motions of the body are

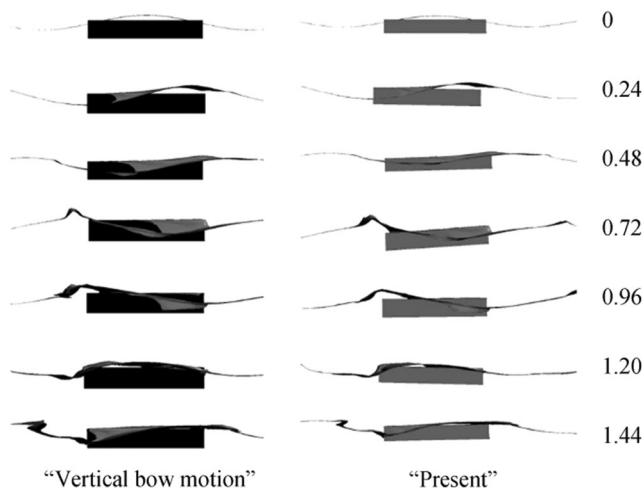


Fig. 26 Visualization of the wave-body kinematics

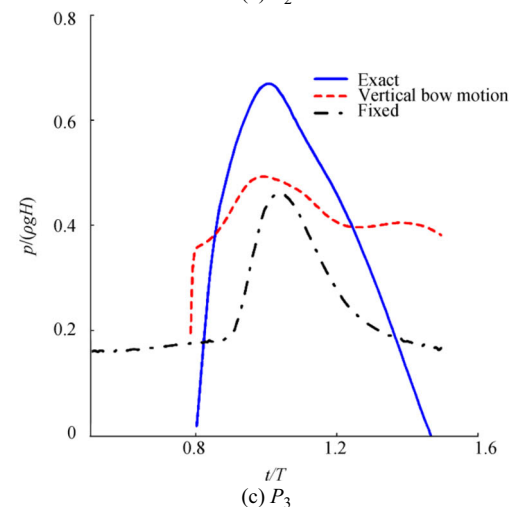
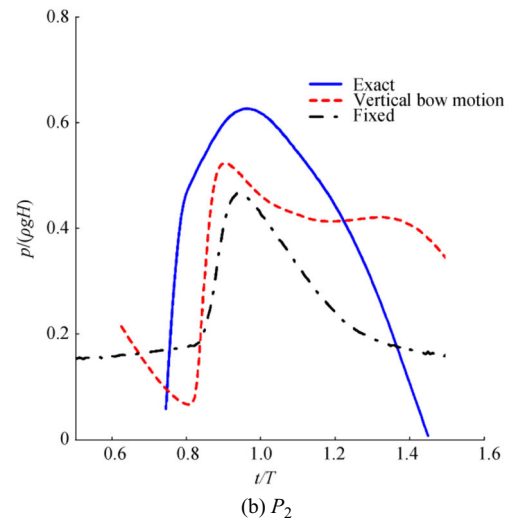
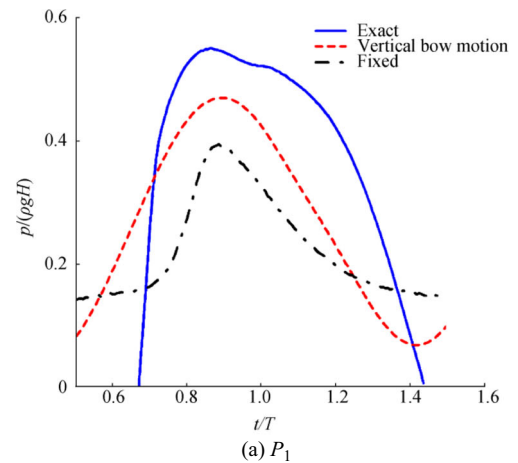


Fig. 27 Green water pressure: a P_1 ; b P_2 ; c P_3

having a phase lag with the incident wave. Therefore, for “Exact” case, the relative velocities would be higher which is responsible for the higher impact load. This study is done for the wave frequency for which the length of the vessel is nearly equal to the wavelength for the steepness ratio of 0.06.

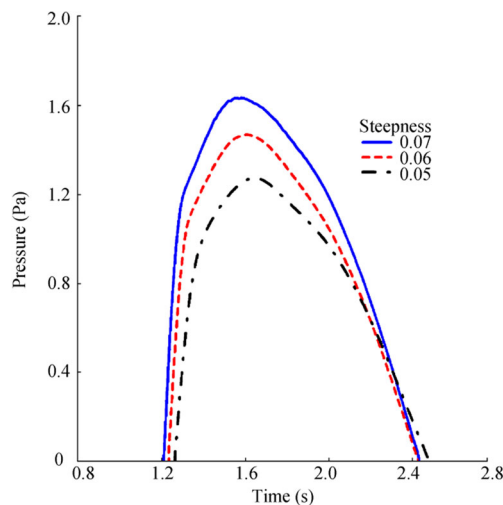


Fig. 28 Comparison of impact load for different steepness at heading angle 180°

However, “Exact” results could also be lower for other wave frequencies. This is because, both the amplitude and phase of motion with respect to the wave changes with wave frequency. This is because the relative bow height depends on the phase between the wave and the body. However, it is evident from Fig. 27 that a significant difference exists between the results obtained considering the vertical bow motion and by considering the coupled heave and pitch motion.

3.4 Effect of Wave Steepness

In the final set of results, the green water impact is calculated for different wave steepness at non-dimensional frequency $\lambda/L \approx 1$ because vessel motions, as well as the vertical bending moment, are most severe around this frequency. The impact pressures are calculated for three values of the steepness factor $H/\lambda = 0.05, 0.06$, and 0.07 . Figure 28 shows the comparison of actual impact load for different steepness at a heading angle of 180° . The impact pressure is found to be higher as steepness increases. Table 8 gives the non-dimensional peak pressure values for the $H/\lambda = 0.05, 0.06$, and 0.07 respectively. From the table, it may be noted that peak pressure increases 15%, if steepness increases from 0.05 to 0.06 and peak pressure increases 10%, if steepness increases from 0.06 to 0.07.

Figure 29 shows the maximum pressure on the deck relative to the hydrostatic pressure for varying steepness. The

Table 8 Pressure peak values for different steepnesses

Steepness	Peak pressure value (Pa)
0.05	1250
0.06	1450
0.07	1600

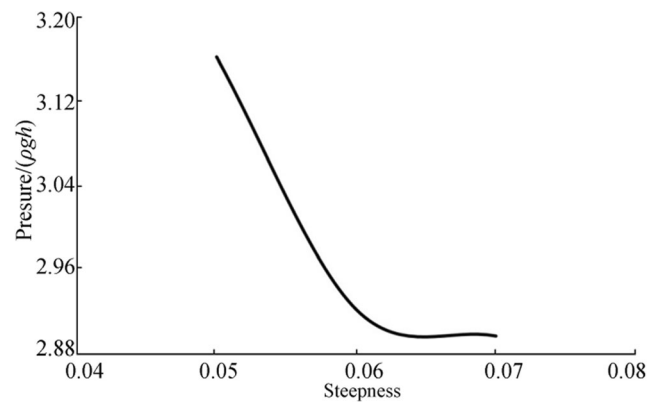


Fig. 29 Maximum pressure relative to the hydrostatic pressure on the deck with respect to the steepness ratio

hydrostatic pressure is expressed as $\rho g H$, where H is the relative deck height. For a low-wave steepness range, the dynamic pressure computed through CFD is much larger than hydrostatic pressure. However, as the wave steepness increases, the hydrostatic pressure increases rapidly, thus decreasing the ratio but the dynamic pressure is still significantly larger than the static pressure.

4 Conclusions

This paper investigates the problem of green water loading for marine vessels by developing a new approach, whereby the effect of body motions on the occurrence of green water may be calculated. The approach is established using extensive comparisons with 2D and 3D numerical results as well as experimental results available in published literature. The results obtained for the 3D body highlight the influence of heave and pitch motions on the green water loading.

For a floating body free to heave and pitch, it is well-known as well as seen from the present results that the phase between body motion and wave always plays an important role. In addition to that, considering actual orientation of the vessel during the impact is also necessary. The combined radiated-diffracted wavefield for the exact case is different from the diffracted wavefield for the fixed cases which lead to the difference in green water pressure even if the phase between body motion and wave are same. Furthermore, from the plots of impact pressure, it can be concluded that effect of bow acceleration is vital in the assessment of green water loading on the deck, which is larger than the static pressure.

The green water loading which includes the static and dynamic loads are affected by many factors like ship vertical motions, fluid static pressure, and flow velocity. The present paper made an attempt to include all the aspects in a relatively simplified way. For example, the present method uses potential flow solver to calculate the body motion without considering the green water load as an external force; thus, the effect

of green water loading on vessel motion is ignored. However, in order to understand this effect, a coupling between the two can be done as a future study. In principle, such coupling is possible as in-house time-domain code is readily available. The present work highlights the importance of vessel motions on green water occurrence which may be important in the design of structural members, especially the bow design of the marine vessel.

References

- Buchner B (1995) The impact of green water on FPSO design. Offshore Technology Conference, Houston, USA
- Buchner B, Cozijn JL (1997) An investigation into the numerical simulation of green water. Proc. Int. Conf. on the Behavior of Offshore Structures, BOSS'97, vol 2, 113–125
- Buchner B, Voogt A (2000) The effect of bow flare angle on FPSO green water loading. Proceedings of ETCE/OMAE2000 Joint Conference Energy for the New Millennium, New Orleans
- Datta R, Fonseca N (2013) Analysis of the forward speed effects on the radiation forces on a fast ferry. Ocean Eng 60:136–148
- Datta R, Rodrigues JM, Guedes Soares C (2011) Study of the motions of fishing vessels by a time domain panel method. Ocean Eng 38(5): 782–792
- De Carvalhoe Silva DF, Rossi RR (2014) Green water loads determination for FPSO exposed to beam sea conditions. 33rd International Conference on Ocean, Offshore and Arctic Engineering, V08BT06A012–V08BT06A012. San Francisco
- Faltinsen OM, Greco M, Landrini M (2002) Green water loading on a FPSO. J Offshore Mech Arct Eng 124(2):97–103
- Gorf P, Barltrop N, Okan B, Hodgson T, Rainey R (2000) FPSO bow damage in steep waves. Rogue Waves 2000 Workshop, Brest, vol 32, 37
- Greco M (2001) A two-dimensional study of green-water loading. PhD. Norwegian University of Science and Technology, Trondheim
- Greco M, Lugni C (2012) 3-D seakeeping analysis with water on deck and slamming. Part 1: numerical solver. J Fluids Struct 33:127–147
- Greco M, Landrini M, Faltinsen OM (2004) Impact flows and loads on ship-deck structures. J Fluids Struct 19(3):251–275
- Greco M, Bouscasse B, Lugni C (2012) 3-D seakeeping analysis with water on deck and slamming. Part 2: experiments and physical investigation. J Fluids Struct 33:148–179
- Greco M, Colicchio G, Lugni C, Faltinsen OM (2013) 3D domain decomposition for violent wave-ship interactions. Int J Numer Methods Eng 95(8):661–684
- Greco M, Lugni C, Faltinsen OM (2014) Can the water on deck influence the parametric roll of a FPSO? A numerical and experimental investigation. Eur J Mech B/Fluids 47:188–201
- Greco M, Lugni C, Faltinsen OM (2015) Influence of motion coupling and nonlinear effects on parametric roll for a floating production storage and offloading platform. Phil Trans R Soc A 373(2033): 20140110
- Hirt CW, Nichols BD (1981) Volume of fluid (VOF) method for the dynamics of free boundaries. J Comput Phys 39(1):201–225
- Kleefsman KT, Loots GE, Veldman AE, Buchner B, Bunnik T, Falkenberg E (2005) The numerical simulation of green water loading including vessel motions and the incoming wave field. 24th International Conference on Offshore Mechanics and Arctic Engineering, Halkidiki, Greece, 981–992
- Le Touze D, Marsh A, Oger G, Guilcher PM, Khaddaj-Mallat C, Alessandrini B, Ferrant P (2010) SPH simulation of green water and ship flooding scenarios. J Hydrodyn Ser B 22(5):231–236
- Lee YG, Kim N, Kang BH, Jeong KL (2009) Numerical simulation of green water incident on bow deck. The Nineteenth International Offshore and Polar Engineering Conference. International Society of Offshore and Polar Engineers 1:495–502. Osaka
- Lee HH, Lim HJ, Rhee SH (2012) Experimental investigation of green water on deck for a CFD validation database. Ocean Eng 42:47–60
- Lu H, Yang C, Löhner R (2012) Numerical studies of green water impact on fixed and moving bodies. Int J Offshore Polar Eng 22(2):123–132
- Nielsen KB, Mayer S (2004) Numerical prediction of green water incidents. Ocean Eng 31(3):363–399
- Park JC, Kim MH, Miyata H (1999) Fully non-linear free-surface simulations by a 3D viscous numerical wave tank. Int J Numer Methods Fluids 29(6):685–703
- Sengupta D, Datta R, Sen D (2016) A simplified approach for computation of nonlinear ship loads and motions using a 3D time-domain panel method. Ocean Eng 117:99–113
- Shibata K, Koshizuka S (2007) Numerical analysis of shipping water impact on a deck using a particle method. Ocean Eng 34(3):585–593
- Tanizawa K, Sawada H, Tsujimoto M, Koshizuka S (2004). Experimental and numerical study of shipping water impact on running ship fore-deck in regular head seas. Hydrodynamics VI: Theory and Applications: Proceedings of the 6th International Conference on Hydrodynamics, Perth, Western Australia, 125
- Theilen L, Dettelsen O, Abdel-Maksoud M, Bohm M (2015) Efficient simulation method to predict green water loads on superstructures. 34th International Conference on Ocean Offshore and Arctic Engineering. Newfoundland, Canada, V001T01A035–V001T01A035
- Voogt A, Buchner B (2004) Prediction of wave impact loads on ship-type offshore structures in steep fronted waves. The Fourteenth International Offshore and Polar Engineering Conference. Toulon, France, ISOPE-I-04-063
- Voogt AJ, Buchner B, Garcia JLC (2004) Wave impact excitation on ship-type offshore structures in steep fronted waves. Proceedings OMAE Speciality Conference on Integrity of Floating Production, Storage & Offloading (FPSO) Systems, Houston, 04-0062
- Zhao X, Ye Z, Fu Y (2014) Green water loading on a floating structure with degree of freedom effects. J Mar Sci Technol 19(3):302–313
- Zhu R, Miao G, Lin Z (2009) Numerical research on FPSOs with green water occurrence. J Ship Res 53(1):7–18
- Zwart PJ, Godin PG, Penrose J, Rhee SH (2007). Ship hull simulations with a coupled solution algorithm. Proceedings of the 10th International Symposium on Practical Designs of Ships and Other Floating Structures, Houston